

Oxygen redox chemistry without excess alkali-metal ions in $\text{Na}_{2/3}[\text{Mg}_{0.28}\text{Mn}_{0.72}]\text{O}_2$

Urmimala Maitra^{a†}, Robert A. House^{a†}, James W. Somerville^a, Nuria Tapia-Ruiz^a, Juan G. Lozano^a, Niccoló Guerrini^a, Rong Hao^a, Kun Luo^a, Liyu Jin^a, Miguel A. Pérez-Osorio^a, Felix Massel^c, David M. Pickup^d, Silvia Ramos^d, Xingye Lu^e, Daniel E. McNally^e, Alan V. Chadwick^d, Feliciano Giustino^a, Thorsten Schmitt^e, Laurent C. Duda^c, Matthew R. Roberts^a, Peter G. Bruce^{ab*}

†joint first author

^aDepartment of Materials, University of Oxford, Parks Road, Oxford OX1 3PH, UK.

^bDepartment of Chemistry, University of Oxford, Parks Road, Oxford OX1 3PH, UK.

^cDepartment of Physics and Astronomy, Division of Molecular and Condensed Matter Physics, Uppsala University, Box 516, S-751 20 Uppsala, Sweden.

^dSchool of Physical Sciences, University of Kent, Canterbury, Kent CT2 7NH, UK.

^eSwiss Light Source, PSI, 5232 Villigen, Switzerland.

ABSTRACT

The search for improved energy-storage materials has revealed Li- and Na-rich intercalation compounds to be promising high-capacity cathodes. They exhibit capacities in excess of what would be expected from alkali-ion removal/reinsertion and charge compensation by transition-metal (TM) ions. The additional capacity is provided through charge compensation by oxygen-redox chemistry and some oxygen loss. It has been reported previously that O-redox occurs in O-2p orbitals that interact with alkali-ions in the transition-metal and alkali-ion layers (that is, O-redox occurs in compounds containing $\text{Li}^+\text{-O}(2p)\text{-Li}^+$ interactions). $\text{Na}_{2/3}[\text{Mg}_{0.28}\text{Mn}_{0.72}]\text{O}_2$ exhibits excess capacity and here we show that this is due to O-redox, despite Mg^{2+} residing in the TM layers rather than alkali-metal ions, demonstrating that excess alkali-metal ions are not required to activate O-redox. We also show that unlike the alkali-rich compounds, $\text{Na}_{2/3}[\text{Mg}_{0.28}\text{Mn}_{0.72}]\text{O}_2$ does not lose O. Extraction of alkali ions from the alkali and TM layers in the alkali-rich compounds results in severely underbonded oxygen, promoting oxygen loss, whereas Mg^{2+} remains in $\text{Na}_{2/3}[\text{Mg}_{0.28}\text{Mn}_{0.72}]\text{O}_2$, stabilising oxygen.

INTRODUCTION

Traditional oxide-based intercalation cathodes for lithium and sodium-ion batteries store charge on the transition-metal ions. For example, on charging the LiMn_2O_4 cathode, Li^+ ions are extracted with charge compensation by oxidation of Mn^{3+} to Mn^{4+} .¹⁻³ It is now recognised that charge can also be stored on the oxide ions by invoking redox chemistry on the oxygens.⁴⁻¹¹ The phenomenon of O-redox is important because it could offer a route to cathodes with increased capacity, by storing charge on the transition-metal and oxide ions.

A number of compounds are known to exhibit O-redox, based on the Li- or Na-rich materials such as $\text{Li}[\text{Li}_{0.2}\text{Ni}_{0.13}\text{Co}_{0.13}\text{Mn}_{0.54}]\text{O}_2$ ⁸ and Na_2IrO_3 ⁹. Unfortunately, these alkali-metal rich compounds also exhibit O-loss from the lattice on charging, which is undesirable in a cathode.^{4,7,8,12-18} The alkali-metal-rich compounds have alkali-metal ions in transition-metal (TM) as well as the alkali-metal (AM) layers and, as a result, the 2p orbitals of the oxygen atoms (O-2p) overlap with the 2s orbitals of the

Li^+ cations from the adjacent TM and AM layers forming $\text{Li}^+\text{-O-Li}^+$ interactions. The relatively ionic nature of these interactions places these O-2p states at the top of the O-valence band, and it is these orbitals, it has been argued, that engage in O-redox.⁴ As a consequence, it is important to explore whether alkali-metal ions on the transition-metal sites are essential and whether they have a unique role in O-redox.

The layered sodium intercalation compound, $\text{Na}_{2/3}[\text{Mg}_{0.28}\text{Mn}_{0.72}]\text{O}_2$, has been reported by Yabuuchi et. al. to have capacity beyond the normal limit of transition-metal oxidation, but without evidence for its origin¹⁹. Whilst the work suggested the possibility that the excess capacity arises from O-redox it raised many important questions about the nature of charge compensation in this material such as: is O-loss observed?; does oxidation to Mn^{5+} occur?; or, do a combination of processes explain what is seen? (Mn^{5+} combined with O-redox has been reported in $\text{Li}_4\text{Mn}_2\text{O}_5$ ²⁰). Understanding the excess capacity in $\text{Na}_{2/3}[\text{Mg}_{0.28}\text{Mn}_{0.72}]\text{O}_2$ is important because, unlike previous excess capacity materials, it contains Mg^{2+} rather than alkali-metal ions in the TM-layers.

Here we show that the $\text{Na}_{2/3}[\text{Mg}_{0.28}\text{Mn}_{0.72}]\text{O}_2$ does exhibit O-redox, therefore alkali-metal ions are not required in the transition-metals' layers in order to promote O-redox. Furthermore, unlike the alkali-metal-rich compounds the $\text{Na}_{2/3}[\text{Mg}_{0.28}\text{Mn}_{0.72}]\text{O}_2$ does not lose oxygen (and no formation of Mn^{5+} was detected). The suppression of O-loss is attributed to Mg^{2+} remaining in the lattice and interacting with O-2p orbitals, whereas in the alkali-metal-rich compounds the alkali-metal ions are removed from the alkali-ion and TM-layers, resulting, at high degrees of deintercalation (high states of charge), in under-coordinated oxygen and non-bonded, electron deficient, O-2p states, leading to oxygen evolution. The suppression of O-loss and promotion of O-redox by Mg^{2+} in the TM-layers points the way to new classes of intercalation cathodes for alkali-ion batteries.

RESULTS

The compound P2 $\text{Na}_{2/3}[\text{Mg}_{0.28}\text{Mn}_{0.72}]\text{O}_2$ prepared here and in previous work¹⁹ is based on a P2 layered $\text{Na}_{2/3}\text{MnO}_2$ where Mn ions have been substituted by Mg. Phase pure samples with 1/3 Mg, and hence all Mn^{4+} , could not be obtained. Powder x-ray diffraction (PXRD) data were used to refine the structure of $\text{Na}_{2/3}[\text{Mg}_{0.28}\text{Mn}_{0.72}]\text{O}_2$, Supplementary Figure 1, confirming that the compound possesses the layered P2 structure. It is composed of oxygen layers stacked in an ABBA arrangement, with Mg and Mn occupying the octahedral sites between the AB oxide layers and Na occupying trigonal prismatic sites between the AA and BB layers, as illustrated in Figure. 1(a). So-called honeycomb ordering of Mg and Mn exists in the TM-layers, similar to that observed between Li and Mn in Li-rich compounds.^{21,22} The central 2b site of the honeycomb is surrounded by 4d sites predominately filled with Mg and Mn respectively, Figure. 1(b). This results in characteristic reflections in the 2θ range of 20 to 28 degrees, which have been included in the refinement in Supplementary Table 1.

The composition of the material was confirmed by inductively coupled plasma optical emission spectroscopy (ICP-OES) and is shown in Supplementary Table 2. The oxidation state of the Mn in the pristine sample was investigated using a magnetic measurement (Supplementary Figure 2), which shows that the Mn oxidation state was $\sim +3.81$, slightly lower than that expected from the nominal composition +3.85. The value of +3.81 is used throughout for calculations of average oxidation state and composition based on the charge passed. The synthesis of $\text{Na}_{2/3}[\text{Mg}_{0.28}\text{Mn}_{0.72}]\text{O}_2$ and characterisation of its structure and composition are described in the supplementary information. The synthesis of sodium transition-metal oxides is often accompanied by the formation of Na_2CO_3 .²³⁻

²⁶ The synthesis procedure used here was developed to mitigate this, and is described in the methods section. Thermo-gravimetric analysis/mass spectrometry (TGA-MS) data of the sample prepared by this method confirms that the material is largely free from Na₂CO₃ impurities (Supplementary Figure 3). Scanning electron microscopy (SEM) images of the material are shown in Supplementary Figure 4, demonstrating plate-shaped particles with diameter of 1-3 μm and thickness 0.5-2 μm, consistent with previous observations¹⁹.

Electrode preparation and cell assembly are described in the methods section. The charge-discharge curves for cells containing Na_{2/3}[Mg_{0.28}Mn_{0.72}]O₂ are shown in Figure 2 and the capacity and average discharge voltage versus cycle number plot in Supplementary Figure 5. The 1st charge in Figure 2 is divided into two regions. Region I corresponds to the initial extraction of ~0.14 Na⁺, charge compensated principally by oxidation of Mn³⁺, from Na_{0.67}[Mg_{0.28}Mn_{0.72}]O₂ to Na_{0.53}[Mg_{0.28}Mn_{0.72}]O₂. Note the measured Mn oxidation state of the pristine was +3.81, which agrees well with the extraction of 0.14 Na to reach Mn⁴⁺ at the end of Region I. Region II, the plateau region, represents capacity beyond the limits of normal transition-metal oxidation. The PXRD data collected in operando at progressive states of charge and discharge are shown in Supplementary Figure 6. There is a small variation of peak positions on initial sodium extraction (region I), corresponding to a continuous solid solution. The plateau (region II), signals 2 phase behaviour and the PXRD data reflect this with the appearance and growth of a peak at 18 degrees in 2θ, which is the most prominent peak associated with the O2 structure. At the end of charge, the average electrode composition, based on charge passed, is Na_{0.14}[Mg_{0.28}Mn_{0.72}]O₂. Assuming, the Na deficient end member of the two phase reaction is Na₀[Mg_{0.28}Mn_{0.72}O]₂, we then would expect a mixture of P2 and O2 phases at the end of charge, as is observed in XRD data presented (Supplementary Figure 6). The P2 to O2 transition in Na intercalation compounds is well known; in the absence of Na⁺ ions between the oxygen-layers to stabilise the trigonal prismatic coordination, the oxygen-layers shear, changing their stacking to ABAC, replacing the trigonal prismatic sites with octahedral sites.²⁷ We have studied further the structure of the charged material using annular dark-field and annular bright field scanning-transmission electron microscopy (ADF-STEM and ABF-STEM), Figure 3. The cations appear as bright and dark spots respectively in the ADF and ABF images. The results show the Mg²⁺ ions do not migrate to the alkali layers. There is a lack of scattering from the AM-layers and the Mg is still evident in the TM-layers at the end of charge, the sequence Mg-Mn-Mn-Mg associated with the cation honeycomb ordering in the TM-layers is highlighted in the Figure by the red ellipse. This indicates that the Mg ions are still present in the TM layer and are neither displaced nor removed from the lattice on charging, in contrast to Li in the Li-rich layered materials where on charging the Li⁺ ions from the TM layers are removed. The conclusion is consistent with that of Yabuuchi et al.¹⁹ who, with synchrotron radiation, were able to resolve the presence of TM-layer ordering for up to 5 cycles in contrast to Li analogues where the Li removal from the Tm layers results in the loss of order.²²

To explore whether oxygen is lost from the lattice and contributes to the Na_{2/3}[Mg_{0.28}Mn_{0.72}]O₂ excess capacity, operando mass spectrometry was carried out. This method permits the analysis of the gases evolved from the electrochemical cell during charge and discharge. The experimental arrangement is described in the methods section. The results are presented in Figure 4. There is no evidence of direct O₂ evolution on charging and only a very small amount of CO₂ is observed, corresponding to just 0.009 moles of CO₂ per mole of the Na_{2/3}[Mg_{0.28}Mn_{0.72}]O₂. There is rapid exchange between gases in the electrolyte and the Ar flow through the cell and any gases dissolved in the electrolyte would only account for < 1% of the charge passed. As discussed previously, oxygen lost from the lattice of an oxide cathode can be released as reduced species, which reacts with the solvent of the electrolyte solution to generate CO₂^{8,15,28,29}. To examine whether the very small amount of CO₂ observed here is generated by O-loss from the lattice, ¹⁸O-labelled

$\text{Na}_{2/3}[\text{Mg}_{0.28}\text{Mn}_{0.72}]\text{O}_2$ was prepared, as described in the methods section, and subjected to operando mass spectrometry, Supplementary Figure 8. No evidence of $^{18}\text{O}_2$ or ^{18}O -labelled CO_2 was observed, consistent with no O-loss from the $\text{Na}_{2/3}[\text{Mg}_{0.28}\text{Mn}_{0.72}]\text{O}_2$ lattice. Although all previous studies of oxygen loss from materials exhibiting excess capacity have shown that CO_2 is evolved, to investigate the possibility of oxygen loss occurring but leading to solution soluble or solid decomposition products without CO_2 , ^{17}O NMR and TGA-MS were carried out. ^{17}O -labelled $\text{Na}_{2/3}[\text{Mg}_{0.28}\text{Mn}_{0.72}]\text{O}_2$ was prepared as for the ^{18}O -labelled material and charged to 4.5 V, the cell was disassembled and the NMR spectrum from the electrolyte examined for the presence of ^{17}O containing species (Supplementary Figure 9). The NMR method would detect the release of as little as 0.2 % of the total oxygen from the material, therefore the lack of any evidence of new ^{17}O species shows no oxygen loss in the form of soluble oxygen containing species has occurred. The TGA-MS data of the ^{18}O -labelled electrode at the end of charging did not show any evidence of additional solid phases, Supplementary Figure 10, indicating that no solid decomposition products are formed containing oxygen evolved from the material. The lack of any oxygen loss from $\text{Na}_{2/3}[\text{Mg}_{0.28}\text{Mn}_{0.72}]\text{O}_2$ is in contrast to previous lithium and sodium O-redox materials containing either 3d or 4d Tm cations and demonstrates that the substitution of alkali-metal ions on the transition-metal sites with Mg suppresses O-loss.^{8,11,15,30–33}

The CO_2 released from the cell does not arise from $\text{Na}_{2/3}[\text{Mg}_{0.28}\text{Mn}_{0.72}]\text{O}_2$, what therefore is its origin? The CO_2 occurs in two regions of the charging curve, Figure 4, the first around 3.5 V and the second at 4.5 V. The first is associated with decomposition of a small amount of Na_2CO_3 and the second is consistent with direct electrolyte oxidation at high voltages^{8,15}. We noted above that Na_2CO_3 is often present with sodium transition-metal oxides and we took special measures to reduce it to a minimum, see SI, but it cannot be eliminated entirely. To demonstrate that the first evolution of CO_2 arises from the small amount of Na_2CO_3 , additional Na_2CO_3 was intentionally added to the electrode. The magnitude of the CO_2 evolved scales with the quantity of Na_2CO_3 , Supplementary Figure 11.

To investigate directly the origin of the extra capacity beyond transition-metal oxidation, a range of spectroscopic techniques were employed including soft x-ray absorption spectroscopy (SXAS), resonant inelastic x-ray scattering (RIXS) and x-ray absorption near edge spectroscopy (XANES). The XANES pre-edge spectra show a small change on extracting Na across region 1, Supplementary Figure 12, consistent with the oxidation state increasing from 3.81 towards 4 in this region. Across the plateau the pre-edge shows no evidence of a significant shift, indicating no contribution from the Mn to charge compensation in this region. SXAS data on charge and discharge are shown in Figure 5 and correspond to electronic transitions from the oxygen 1s to empty states just above the Fermi level. The two peaks that dominate the spectra up to 533 eV in the pristine material are expected for transitions from the oxygen 1s to empty Mn 3d states mixed with O-2p states, as discussed previously for Mn rich materials^{8,15} and is consistent with a MnO_2 standard as shown. Changes in the area under the spectra in Figure 5(b) are shown in Figure 5(c) and correspond to changes in the density of empty states just above the Fermi level (528 to 532 eV). When charging the material through region 1 the increase in density of empty states is due to the oxidation of Mn. The density of empty states continues to increase as the material is charged through Region II in good agreement with the charge extracted, Figure 5(c). This increase cannot be explained through further oxidation of Mn since the Mn XANES data shows negligible changes in this region. Therefore the increase seen when x has dropped below ~ 0.53 in $\text{Na}_x\text{Mg}_{0.28}\text{Mn}_{0.72}\text{O}_2$ must correspond to the removal of electrons from oxygen and the creation of electron hole states on the O. The electronic structure on the oxygen was probed further with RIXS, Figure 5(d). There is clear evidence of a change in the spectral weight across the plateau region. These changes are consistent with what we observed previously for $\text{Li}[\text{Li}_{0.2}\text{Ni}_{0.13}\text{Co}_{0.13}\text{Mn}_{0.54}]\text{O}_2$ ⁸ and $\text{Li}[\text{Li}_{0.2}\text{Ni}_{0.2}\text{Mn}_{0.6}]\text{O}_2$ ¹⁵. On discharge, the oxygen hole states are

repopulated as shown in Region III in Figure 5(c). The capacity on discharge exceeds slightly that on charge, consistent with some Mn^{4+} being reduced to Mn^{3+} , Supplementary Figure 12. As can be seen from Supplementary Figure 12, the position of Mn edge remains predominately unchanged during discharge until ~ 2.3 V, however, at the end of discharge the Mn is reduced to $\sim +3.7$ and accounts for $\sim 0.2 e^-$ of charge passed. The discharge corresponds to $\sim 0.6 e^-$ per formula unit and therefore the charge which cannot be accounted for by Mn reduction ($\sim 0.4 e^-$) must be charge compensated by oxygen reduction matching the degree of oxygen oxidation seen on charge and the changes seen in the oxygen SXAS on discharge. The experimental density of hole states seems further reduced than anticipated on discharge compared to pristine. SXAS, although not explicitly a surface technique in the collection mode used (fluorescence), is comparatively sensitive to electronic structure in the near-surface fraction of these 1-3 μm diameter particles. As Na intercalation starts from the surface, the surface or near surface regions can become somewhat over reduced, resulting in fewer hole states near the surface than predicted based on the average composition. This may also be related to the O2 to P2 transition.

Considering discharge after the 1st charge, there is a significant difference between the charge and discharge voltages. Significant voltage differences, e.g. ~ 400 mV, have been observed previously in other Na intercalation compounds, associated with the transition between O2 or OP4 structures and P2.^{27,34,35} The reason for these differences is not known and a detailed study of the mechanism of the transformation, including the investigation of materials that exhibit large as well as those that exhibit small differences would be needed to understand the origin. It is noteworthy that although the P2 phase is reformed on discharge, there are significant stacking faults in the P2 phase after one cycle compared with the pristine $\text{Na}_{2/3}[\text{Mg}_{0.28}\text{Mn}_{0.72}]\text{O}_2$. The peaks in the PXRD pattern broaden and the STEM data show evidence for many stacking faults (Supplementary Figure 7). Although Raman spectroscopy, Supplementary Figure 13, showed no evidence of true peroxide (O-O distance 1.4 Å), this does not rule out distortions of the oxygen sublattice. Such distortions have been reported in other O-redox materials.¹⁰ The Mn XANES pre-edge intensity changes on charge-discharge indicative of displacements of the oxygen around Mn associated with O-redox. Such oxygen displacements and the stacking faults represent structural changes that may be associated with the changes in the voltage curve on discharge. It is important to note that despite the evidence for some degree of oxygen displacement, the Mg and Mn cations remain in their sites in the TM-layers. On cycling the plateau region shortens somewhat. The changes are less dramatic but reminiscent of those seen in lithium rich layered materials. In the present case the shortening of the plateau is not associated with oxygen loss but may be related to the structural changes and O2 to P2 transformation just discussed. It is important to note that the present paper focusses on the 1st charge behavior. Understanding discharge/cycling and the role of the P2-O2 transformation are subjects for further study.

DISCUSSION

The P2 structure of $\text{Na}_{2/3}[\text{Mg}_{0.28}\text{Mn}_{0.72}]\text{O}_2$ is stabilised by the presence of the Na^+ ions in the trigonal prismatic sites. On deintercalation, the lower Na content favours shearing of the oxide layers to form the O2 structure, via a two phase reaction. As a result, the electron deficient oxide ions (i.e. the holes on O) in the O2 structure are coordinated octahedrally on one side by 1 Mg^{2+} and 2 Mn^{4+} from the TM-layer and on the other side by 3 vacancies when the Na content is zero, as shown in Figure 6(a). We do not observe any Mg extraction or displacement to the AM-layers as Na is deintercalated, the Mg remain in their sites in the TM-layers. The holes on oxygen are located in the 2p orbitals that interact directly with the Mg^{2+} 3s and Mn^{4+} 3d orbitals, Figure 6(a).

Work on the layered alkali-rich compounds that exhibit O-redox, e.g. $\text{Li}[\text{Li}_{0.2}\text{Ni}_{0.13}\text{Co}_{0.13}\text{Mn}_{0.54}]\text{O}_2$, has demonstrated the important role of the alkali-metal ions in the TM-layers. Their presence results in $\text{Li}^+ - \text{O}2\text{p} - \text{Li}^+$ interactions, involving Li^+ from the transition-metal and AM-layers, and the relatively ionic nature of the interactions places these O-2p states at the top of the O-valence band relative to the O-2p states that interact with Ni, Co and Mn i.e. the alkali-ions in the TM-layers promote O-redox in these materials⁴. The results presented here show that Mg^{2+} in the TM-layers also results in O-redox and that alkali-metal ions are not essential to promote O-redox. The O-2p orbitals in $\text{Na}_{2/3}[\text{Mg}_{0.28}\text{Mn}_{0.72}]\text{O}_2$ interact with 1 Mg^{2+} and 2 Mn^{4+} , Figure 6(a). If we take the Mg^{2+} 3s interaction with O-2p, the 3s states are relatively high in energy compared with O-2p, resulting in weak, ionic, Mg-O bonding and, similarly to Li-O, placing the O-2p states relatively high in energy and accessible within the stability window of the electrolyte. In contrast, strongly covalent M-O interactions would push the O-2p states down in energy, Supplementary Figure 14 (showing a schematic of the M-O interactions). We have carried out calculations of the electronic structure of $\text{Na}_{2/3}[\text{Mg}_{1/3}\text{Mn}_{2/3}]\text{O}_2$, the results are presented in Supplementary Figure 15. The procedure is described in the supplementary information. The calculations show that the O-2p states at the top of the valence band. The schematic band diagram Figure 6(b) is derived from the calculated density of states in Supplementary Figure 15.

$\text{Na}_{2/3}[\text{Mg}_{0.28}\text{Mn}_{0.72}]\text{O}_2$ does not exhibit O-loss, in contrast to the alkali-metal rich transition-metal oxides such as $\text{Li}[\text{Li}_{0.2}\text{Ni}_{0.13}\text{Co}_{0.13}\text{Mn}_{0.54}]\text{O}_2$ and Na_2IrO_3 . In alkali rich compounds, alkali-metal ions are removed from both the transition-metal and AM-layers simultaneously on deintercalation. For example, nuclear magnetic resonance (NMR) data for $\text{Li}[\text{Li}_{1/9}\text{Ni}_{1/3}\text{Mn}_{5/9}]\text{O}_2$ ³⁶ and $\text{Na}_{0.8}[\text{Li}_{0.12}\text{Ni}_{0.22}\text{Mn}_{0.66}]\text{O}_2$ ³⁷ show depopulation of the Li in the TM-layers. As a result, at high degrees of deintercalation (high states of charge) corresponding to compositions more Li deficient than $[\text{Li}_{0.2}\text{Ni}_{0.13}\text{Co}_{0.13}\text{Mn}_{0.54}]\text{O}_2$, some of the oxygen will be under-coordinated with oxygen being coordinated by only two cations in the alkali-rich compounds, Figure 6(c). The under-coordination results in non-bonded O-2p orbitals, Figure 6(c) (i.e. O-2p orbitals that no longer interact directly with any cations). These non-bonded O-2p states will be at a higher energy compared with the other oxygen states and are where the holes on oxygen will be concentrated. Such under-coordinated and electron-deficient oxygen will be unstable in the lattice leading to oxygen evolution. It is at just these highly Li deficient compositions (i.e. less than 0.2 Li per formula unit) where we see the charge capacity dominated by oxygen evolution from the lattice rather than O-redox⁸. This is also in accord with a recent suggestion that under-coordinated oxygen more easily forms O-O species¹⁰, a necessary precursor to O_2 evolution. In contrast, in $\text{Na}_{2/3}[\text{Mg}_{0.28}\text{Mn}_{0.72}]\text{O}_2$, oxygen is always coordinated by at least 3 cations and all O-2p orbitals interact with at least 1 cation. The absence of non-bonding and highly electron-deficient O-2p states, even at high levels of deintercalation in $\text{Na}_{2/3}[\text{Mg}_{0.28}\text{Mn}_{0.72}]\text{O}_2$, in contrast to the alkali-metal rich compounds, is consistent with the observation of no O-loss.

CONCLUSIONS

The presence of O-redox in compounds with Mg^{2+} rather than alkali-ions in the TM-layers, demonstrates that alkali-metal ions on the TM layers (and hence an alkali/transition-metal ratio >1) are not essential for a compound to exhibit O-redox. Furthermore, the presence of Mg^{2+} instead of alkali-metal ions suppresses O-loss, in contrast to alkali-rich compounds. This material clearly has drawbacks such as large voltage hysteresis and, as for other 3d O-redox compounds, the excess capacity is at a potential on charge close to the limits of stability for current electrolytes, which limits its implementation in practical systems. However, the results presented here do advance our fundamental understanding of O-redox and its associated extra capacity, especially the structural/compositional features necessary for a material to exhibit O-redox and to suppress O-loss.

Suppressing oxygen loss is important if the true potential of O-redox materials as higher capacity cathodes is to be realised.

METHODS SECTION

Synthesis $\text{Na}_{0.67}\text{Mg}_{0.28}\text{Mn}_{0.72}\text{O}_2$ was synthesized by solid-state reaction between stoichiometric amounts of Na_2CO_3 (Aldrich, $\geq 99.0\%$), MgO (Aldrich, $\geq 99.99\%$) and Mn_2O_3 (Aldrich, $\geq 99.9\%$). The precursors were ball-milled for 2 hr at a rotation rate of 400 rpm. This mixture was then heated at $800\text{ }^\circ\text{C}$ for 10 hours under flowing oxygen and the product slowly cooled to room temperature at $5\text{ }^\circ\text{C min}^{-1}$ under oxygen. The resulting product contained a small amount of carbonate consistent with earlier reports on similar Na transition-metal oxides after synthesis^{23,26}. To eliminate the carbonate residue the as-synthesised powder, prepared as previously described, was transferred immediately to a glove box and reground prior to the application of a second heating step to $700\text{ }^\circ\text{C}$ under an Ar atmosphere at $10\text{ }^\circ\text{C min}^{-1}$ and immediately cooled by quenching under Ar. The material was transferred to an Ar filled glove-box and stored under Ar without any exposure to air. The TGA-MS data in Supplementary Figure 3 show no evidence of the carbonate. ^{18}O and ^{17}O -labelled $\text{Na}_{0.67}\text{Mg}_{0.28}\text{Mn}_{0.72}\text{O}_2$ was prepared by the same method except for the first heating step where the reaction was carried out in a sealed atmosphere of $^{18}\text{O}_2$ or $^{17}\text{O}_2$ -gas (BOC 99.9%) instead of flowing oxygen gas.

Further details about the electrode preparation, electrochemical methods, XRD, DEMS, ICP, XANES, SXAS, RIXS, NMR, TGA-MS, Raman spectroscopy and STEM analysis are provided in the methods section in the supplementary information. Refined cell parameters obtained from powder XRD are include as Table 1 in Supplementary information. All other relevant data are provided in the supplementary information or can be obtained from the authors on request.

Computational Methods Structural and electronic properties were investigated using density functional theory (DFT) as implemented in the Quantum ESPRESSO package.⁷ We employed the generalized gradient approximation of Perdew, Burke, and Ernzerhof (PBE) to the exchange and correlation functional.⁸ We described the core-valence interaction by means of norm-conserving pseudopotentials.⁹ The electron wave functions and charge density were represented by a plane wave basis set using an energy cut off of 100 Ry. The Brillouin zone was sampled using a $3 \times 3 \times 3$ Monkhorst-Pack k-point grid. In order to correctly describe the energetics of the Mn 3d states, we introduced Hubbard corrections in our calculations using the simplified rotational-invariant formulation by Cococcioni and de Gironcoli.¹⁰ A Hubbard U parameter of 4 eV was used, similar to what is reported for other closely related compounds.^{11,12} Spin polarisation was included in our calculations. A $2 \times 2 \times 1$ supercell of the closely related compound $\text{Na}_{2/3}[\text{Mg}_{1/3}\text{Mn}_{2/3}]\text{O}_2$, containing 88 atoms and with "large zig zag" ordering of the Na proposed by Lee et. al.,¹¹ was relaxed until forces on the atoms were less than 0.08 eV/\AA and the total stresses of the unit cell were less than 0.5 kbar. Despite the slightly different composition, the relaxed unit cell parameters match extremely well with our experimental parameters obtained from Rietveld refinement for $\text{Na}_{2/3}[\text{Mg}_{0.28}\text{Mn}_{0.72}]\text{O}_2$ (see Supplementary Table 3). The total and projected density of states were calculated for this optimised structure and the results are shown in Supplementary Figure 15. Relaxed structural model will be available from the authors on request.

Data Availability

The data that support the findings of this study are available from the corresponding author upon request. Correspondence and requests for materials should be addressed to P.G.B.

Competing Interests

The authors declare no competing financial interests.

Author contributions

U.M., R.A.H. and M.R.R. contributed to all aspects of the research. L.C.D., N.G., J.W.S., F.M., K.L., R.H., L.J., U.M., D.E.M., X.L. and T.S. contributed to the measurement SXAS and RIXS spectroscopy. D.M.P., N.T.R., S.R., and A.V.C. contributed to the data collection and analysis of hard XAS measurements. J.W.S., M.P. and F.G. performed the DFT calculations. J.L. collected, processed and interpreted the STEM images. P.G.B., U.M., R.A.H., J.W.S., M.R.R. and L.C.D. interpreted the data. P.G.B. wrote the paper with contributions from U.M., R.A.H, and M.R.R. The project was supervised by P.G.B.

Acknowledgements

P.G.B. is indebted to the Engineering and Physical Sciences Research Council, including the SUPERGEN program, for financial support. We additionally thank the EPSRC for the grant, EP/K040375/1, for the 'South of England Analytical Electron Microscope'. The authors thank Dr. Nitesh Kumar, Maxplanck Institute of Chemical Physics, Dresden for help with magnetic measurements. Synchrotron radiation experiments have been performed at the ADRESS beamline of the Swiss Light Source at the Paul Scherrer Institut, Switzerland. We acknowledge technical and experimental support at the ADRESS beamline by Leonard Nue and Marcus Dantz. Part of this research has been funded by the Swiss National Science Foundation through the Sinergia network Mott Physics Beyond the Heisenberg (MPBH) model and the NCCR MARVEL. The research leading to these results has received funding from the European Community's Seventh Framework Programme (FP7/2007-2013) under Grant Agreement No. 290605 (CO-FUND: PSIFELLOW). The Advanced Light Source is supported by the Director, Office of Science, Office of Basic Energy Sciences, US Department of Energy, under Contract No. DE-AC02-05CH11231. The authors are also grateful to G. Cibir for contributing to the collection of hard XAS data.

Figure Captions

Figure 1. Structure of $\text{Na}_{2/3}[\text{Mg}_{0.28}\text{Mn}_{0.72}]\text{O}_2$. (a) Schematic of the P2 structure showing the stacking sequence of the MO_2 layers, (b) shows the in-plane honeycomb ordering in the transition-metal (TM) layer where the Mg sits in the center of the honeycomb surrounded by Mn ions. Structures were prepared using VESTA.

Figure 2. Electrochemical behavior of $\text{Na}_{2/3}[\text{Mg}_{0.28}\text{Mn}_{0.72}]\text{O}_2$. Galvanostatic charge-discharge curves for $\text{Na}_{2/3}[\text{Mg}_{0.28}\text{Mn}_{0.72}]\text{O}_2$ showing the first 3 cycles (black, red and blue from the 1st to 3rd cycle respectively) at a rate of 10 mA g^{-1} . Indicated with arrows are two distinct regions on charging, the first (I) corresponds to approximately the capacity expected from oxidation of Mn and the second (II) to additional capacity from anionic charge compensation. A third (III) region indicates the discharge.

Figure 3. Scanning tunneling electron microscopy images showing the structure of the charged $\text{Na}_{2/3}[\text{Mg}_{0.28}\text{Mn}_{0.72}]\text{O}_2$ a) ADF-STEM and b) ABF-STEM micrographs of charged $\text{Na}_{2/3}[\text{Mg}_{0.28}\text{Mn}_{0.72}]\text{O}_2$ viewed along the ab plane. Cations appear as light spots in a) and dark in b). The Fast Fourier Transform (inset in (a)) and the atomic arrangement observed are consistent with those of the O2 type material along the [1-10] direction. In (c) an atomic model of the same O2 materials along the [1-10] crystallographic direction is displayed for comparison. The appearance of fully occupied transition metal sites in the ABF images as opposed to the periodic differences seen in the ADF image confirms that Mg ions do not move from the transition metal layer during sodium deintercalation.

Figure 4. Gas loss of $\text{Na}_{2/3}[\text{Mg}_{0.28}\text{Mn}_{0.72}]\text{O}_2$ during electrochemical (de)sodiation. Operando mass spectrometry data collected during the first cycle of $\text{Na}_{2/3}[\text{Mg}_{0.28}\text{Mn}_{0.72}]\text{O}_2$. Top panel shows the electrochemical response of the cell and the bottom panel shows the O_2 and CO_2 gases evolved as a function of the state of charge. No oxygen gas could be detected during cycling, and only a negligible 0.009 moles of CO_2 per mole of $\text{Na}_{2/3}[\text{Mg}_{0.28}\text{Mn}_{0.72}]\text{O}_2$ were observed.

Figure 5. O K-edge Soft x-ray absorption spectroscopy and resonant inelastic x-ray spectroscopy of $\text{Na}_{2/3}[\text{Mg}_{0.28}\text{Mn}_{0.72}]\text{O}_2$. (a) First cycle charge-discharge load curve with points indicating the states of charge **a-g** where SXAS and RIXS data were collected. (b) SXAS O K-edge spectra collected at different states of charge in total fluorescence yield mode. (c) Variation of the density of states in the low energy region (below 533 eV) of the O K-edge SXAS during the first cycle showing a corresponding increase and decrease in hole states on charging and discharging. (d) RIXS on O K-edge of $\text{Na}_{2/3}[\text{Mg}_{0.28}\text{Mn}_{0.72}]\text{O}_2$ with an excitation energy of 531.5 eV showing the growth of the peak at 523 eV across the plateau representing an emission from the O-2p valance band. The inelastic peaks show a general broadening in the samples **a-c**. There are two visibly distinct peaks in the RIXS spectra for samples **d** and **e** in region II implying a change in the electronic distribution around O-sites. The RIXS spectra return to a similar profile as in the pristine material after discharging to **f** and **g**. (Data were collected at Swiss light source, PSI³⁸⁻⁴⁰)

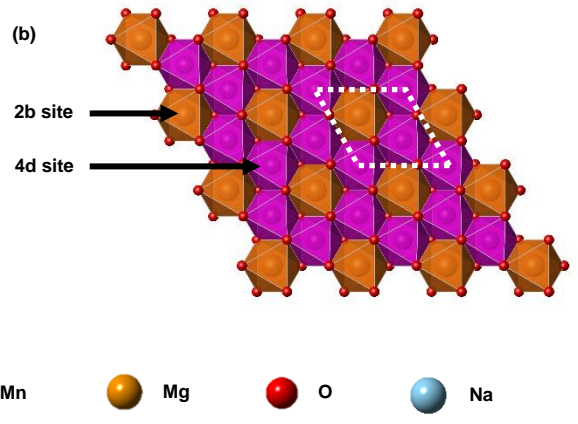
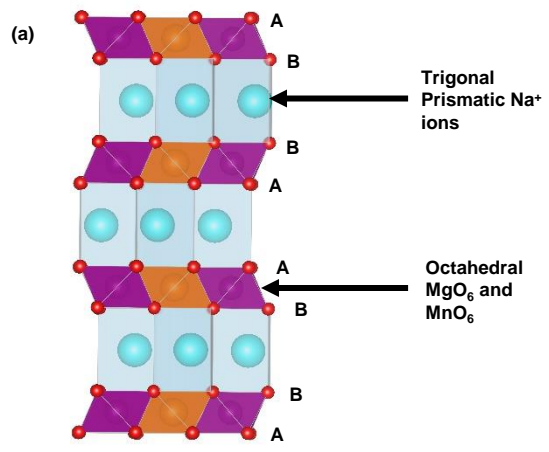
Figure 6. Coordination around oxygen and O-2p orbitals. (a) Left – O2 structure of the sodium deficient phase $\text{Na}_0[\text{Mg}_{0.28}\text{Mn}_{0.72}]\text{O}_2$. Mg and Mn in the octahedral sites in the transition-metal layers shown by orange and purple octahedra respectively. The layers of translucent octahedra represent the vacant Na sites. Red spheres represent oxygen. Right - coordination around oxygen in the O2 structure of $\text{Na}_0[\text{Mg}_{0.28}\text{Mn}_{0.72}]\text{O}_2$, where oxygen is coordinated octahedrally by 2 Mn and 1 Mg from the transition-metal layer and 3 vacancies from the alkali-metal-ion layer. (b) Schematic illustrating the energy versus density of states in the sodium deficient phase of $\text{Na}_0[\text{Mg}_{0.28}\text{Mn}_{0.72}]\text{O}_2$, (c) Left – O3 structure of the lithium deficient phase $\text{Li}_0[\text{Li}_x\text{Ni}_{0.13}\text{Co}_{0.13}\text{Mn}_{0.54}]\text{O}_2$, $x < 0.2$. Li and $(\text{Ni}_{0.13}\text{Co}_{0.13}\text{Mn}_{0.54})$ in the octahedral sites in the transition-metal layers shown by blue and green octahedra respectively. The layers of translucent octahedra represent the vacant Na sites. Red spheres represent oxygen. (c) Right coordination around oxygen in an alkali-rich compound where all alkali-metal ions have been removed ($x = 0$) to leave an oxygen with only 2 coordinating cations and a completely non-bonded O-2p orbital (red). Other O-2p orbitals shown in green. Structural figures were prepared using VESTA.

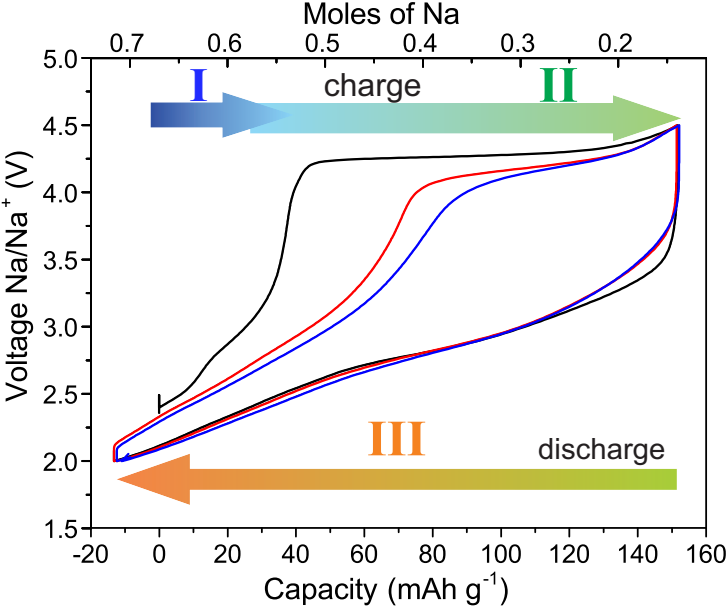
References

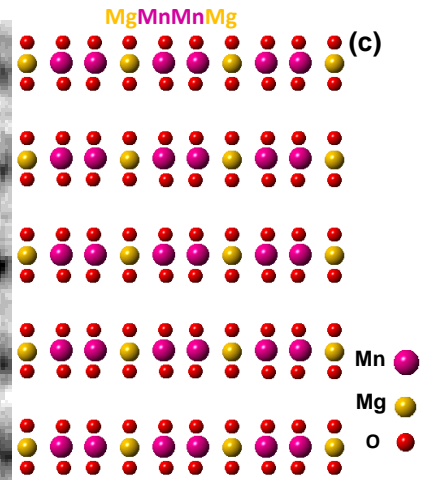
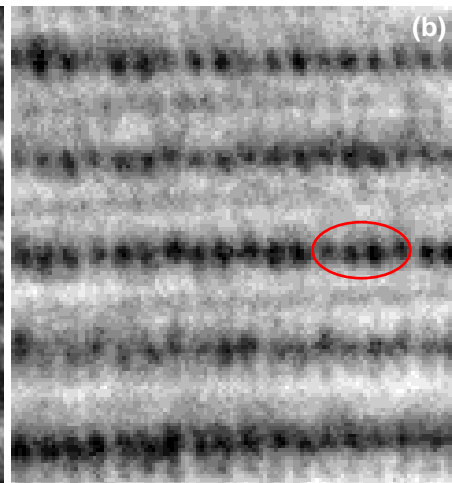
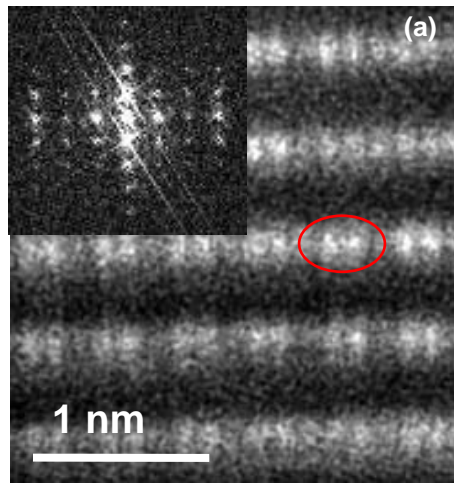
1. Whittingham, M. S. Lithium Batteries and Cathode Materials. *Chem. Rev.* **104**, 4271–4302 (2004).
2. Croguennec, L. & Palacin, M. R. Recent achievements on inorganic electrode materials for lithium-ion batteries. *J. Am. Chem. Soc.* **137**, 3140–3156 (2015).
3. Larcher, D. & Tarascon, J.-M. Towards greener and more sustainable batteries for electrical energy storage. *Nat. Chem.* **7**, 19–29 (2015).
4. Seo, D.-H. *et al.* The structural and chemical origin of the oxygen redox activity in layered and cation-disordered Li-excess cathode materials. *Nat. Chem.* **8**, 692–697 (2016).
5. Lu, Z. & Dahn, J. R. The Effect of Co Substitution for Ni on the Structure and Electrochemical Behavior of T2 and O2 Structure $\text{Li}_{2/3}[\text{Co}_x\text{Ni}_{1/3-x}\text{Mn}_{2/3}]\text{O}_2$. *J. Electrochem. Soc.* **148**, A237 (2001).
6. Kim, J.-S. *et al.* Electrochemical and Structural Properties of $x\text{Li}_2\text{M}'\text{O}_3 \cdot (1-x)\text{LiMn}_{0.5}\text{Ni}_{0.5}\text{O}_2$ Electrodes for Lithium Batteries ($\text{M}' = \text{Ti, Mn, Zr}$; $0 \leq x \leq 0.3$). *Chem. Mater.* **16**, 1996–2006 (2004).
7. Koga, H. *et al.* Different oxygen redox participation for bulk and surface: A possible global explanation for the cycling mechanism of $\text{Li}_{1.20}\text{Mn}_{0.54}\text{Co}_{0.13}\text{Ni}_{0.13}\text{O}_2$. *J. Power Sources* **236**, 250–258 (2013).
8. Luo, K. *et al.* Charge-compensation in 3d-transition-metal-oxide intercalation cathodes through the generation of localized electron holes on oxygen. *Nat. Chem.* **8**, 684–691 (2016).
9. Perez, A. J. *et al.* Strong oxygen participation in the redox governing the structural and electrochemical properties of Na-rich layered oxide Na_2IrO_3 . *Chem. Mater.* (2016).
10. McCalla, E. *et al.* Visualization of O-O peroxo-like dimers in high-capacity layered oxides for Li-ion batteries. *Science* **350**, 1516–21 (2015).
11. Sathiya, M. *et al.* Reversible anionic redox chemistry in high-capacity layered-oxide electrodes. *Nat. Mater.* **12**, 827–35 (2013).
12. Saubanère, M., McCalla, E., Tarascon, J.-M. & Doublet, M.-L. The intriguing question of anionic redox in high-energy density cathodes for Li-ion batteries. *Energy Environ. Sci.* (2015).
13. Koga, H. *et al.* Reversible Oxygen Participation to the Redox Processes Revealed for $\text{Li}_{1.20}\text{Mn}_{0.54}\text{Co}_{0.13}\text{Ni}_{0.13}\text{O}_2$. *J. Electrochem. Soc.* **160**, A786–A792 (2013).
14. Oishi, M. *et al.* Direct observation of reversible charge compensation by oxygen ion in Li-rich manganese layered oxide positive electrode material, $\text{Li}_{1.16}\text{Ni}_{0.15}\text{Co}_{0.19}\text{Mn}_{0.50}\text{O}_2$. *J. Power Sources* **276**, 89–94 (2015).
15. Luo, K. *et al.* Anion Redox Chemistry in the Cobalt Free 3d Transition-metal Oxide Intercalation Electrode $\text{Li}[\text{Li}_{0.2}\text{Ni}_{0.2}\text{Mn}_{0.6}]\text{O}_2$. *J. Am. Chem. Soc.* **138**, 11211–11218 (2016).
16. Rozier, P. *et al.* Anionic redox chemistry in Na-rich $\text{Na}_2\text{Ru}_{1-y}\text{Sn}_y\text{O}_3$ positive electrode material for Na-ion batteries. *Electrochem. commun.* **53**, 29–32 (2015).
17. Du, K. *et al.* Exploring Reversible Oxidation of Oxygen in a Manganese Oxide. *Energy Environ. Sci.* **6**, 3–5 (2016).
18. Castel, E., J. Berg, E., El Kazzi, M., Novák, P. & Villevieille, C. Differential electrochemical mass spectrometry study of interface of $x\text{Li}_2\text{MnO}_3 \cdot (1-x)\text{LiMO}_2$ ($\text{M} = \text{Ni, Co, Mn}$) material as positive electrode in Li-ion batteries. *Chem. Mater.* **2**, 140812152134005 (2014).
19. Yabuuchi, N. *et al.* A new electrode material for rechargeable sodium batteries: P2-type Na

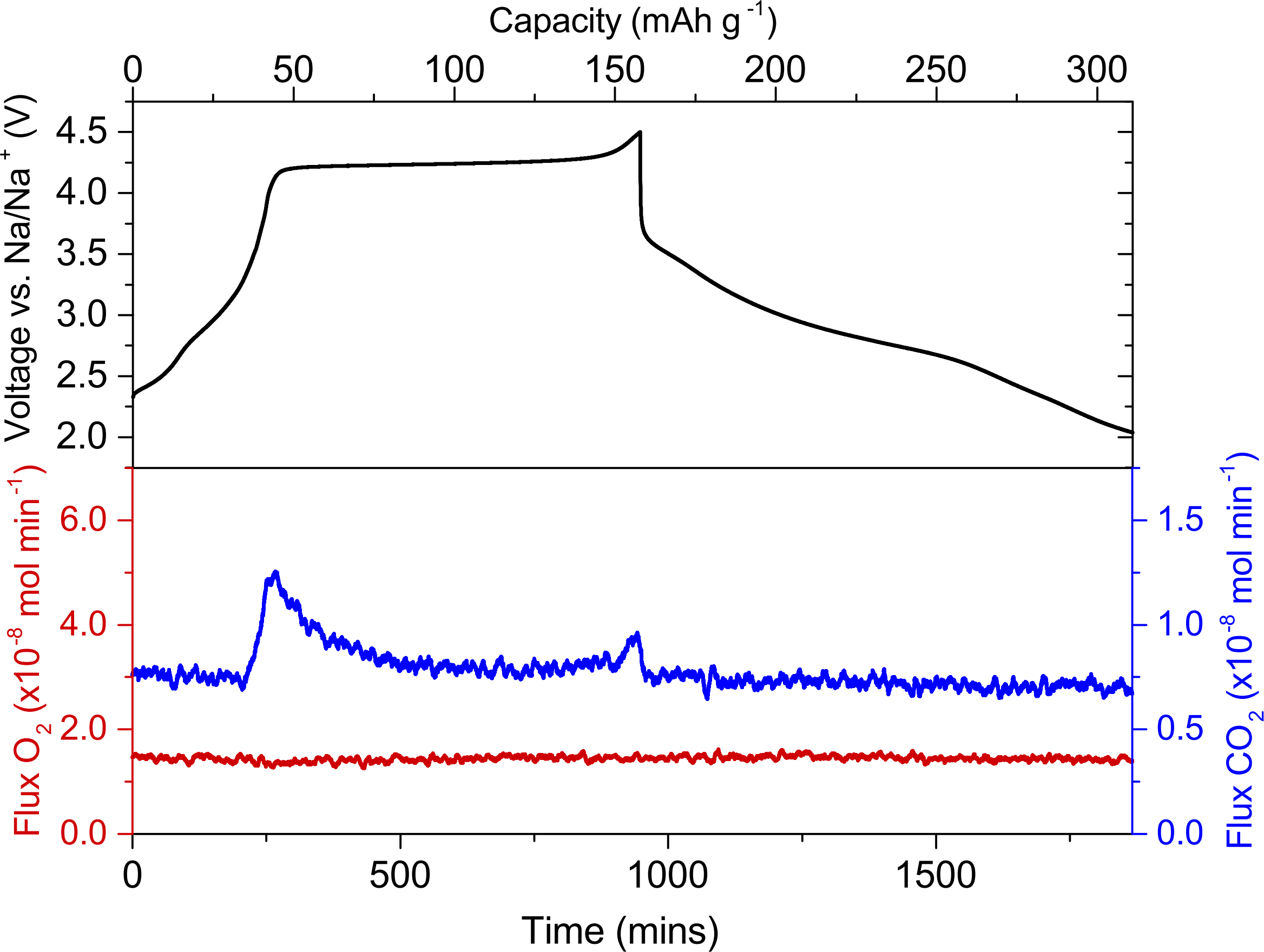
- 2/3 [Mg_{0.28} Mn_{0.72}]O₂ with anomalously high reversible capacity. *J. Mater. Chem. A* **2**, 16851–16855 (2014).
20. Freire, M. *et al.* A new active Li–Mn–O compound for high energy density Li-ion batteries. *Nat. Mater.* **15**, 173–177 (2015).
 21. Meng, Y. S. *et al.* Cation Ordering in Layered O₃ Li[Ni_x Li_{1/3 - 2x/3} Mn_{2/3 - x/3}]O₂ (0 ≤ x ≤ 1/2) Compounds. *Chem. Mater.* **17**, 2386–2394 (2005).
 22. Yabuuchi, N. *et al.* New O₂/P₂-type Li-Excess Layered Manganese Oxides as Promising Multi-Functional Electrode Materials for Rechargeable Li/Na Batteries. *Adv. Energy Mater.* **4**, n/a–n/a (2014).
 23. Stoyanova, R. *et al.* Stabilization of over-stoichiometric Mn⁴⁺ in layered Na_{2/3}MnO₂. *J. Solid State Chem.* **183**, 1372–1379 (2010).
 24. Zhou, T., Zhang, D., Button, T. W., Wright, A. J. & Greaves, C. Influence of cooling rate on the structure and composition of Na_xCoO₂ (x ~ 0.65). *J. Mater. Chem.* **19**, 1123 (2009).
 25. Sathiya, M., Hemalatha, K., Ramesha, K., Tarascon, J.-M. & Prakash, A. S. Synthesis, Structure, and Electrochemical Properties of the Layered Sodium Insertion Cathode Material: NaNi_{1/3}Mn_{1/3}Co_{1/3}O₂. *Chem. Mater.* **24**, 1846–1853 (2012).
 26. Duffort, V., Talaie, E., Black, R. & Nazar, L. F. Uptake of CO₂ in Layered P₂-Na_{0.67}Mn_{0.5}Fe_{0.5}O₂: Insertion of Carbonate Anions. *Chem. Mater.* **27**, 2515–2524 (2015).
 27. Lu, Z. & Dahn, J. R. In Situ X-Ray Diffraction Study of P₂-Na_{2/3}[Ni_{1/3}Mn_{2/3}]O₂. *J. Electrochem. Soc.* **148**, A1225 (2001).
 28. Hong, J. *et al.* Critical Role of Oxygen Evolved from Layered Li-Excess Metal Oxides in Lithium Rechargeable Batteries. *Chem. Mater.* **24**, 2692–2697 (2012).
 29. Aurbach, D. The Correlation Between Surface Chemistry, Surface Morphology, and Cycling Efficiency of Lithium Electrodes in a Few Polar Aprotic Systems. *J. Electrochem. Soc.* **136**, 3198 (1989).
 30. McCalla, E. *et al.* Understanding the Roles of Anionic Redox and Oxygen Release during Electrochemical Cycling of Lithium-Rich Layered Li₄FeSbO₆. *J. Am. Chem. Soc.* **137**, 4804–4814 (2015).
 31. de la Llave, E. *et al.* Improving Energy Density and Structural Stability of Manganese Oxide Cathodes for Na-ion Batteries by Structural Lithium Substitution. *Chem. Mater.* [acs.chemmater.6b04078](https://doi.org/10.1021/acs.chemmater.6b04078) (2016).
 32. Sathiya, M. *et al.* High Performance Li₂Ru_{1-y}Mn_yO₃ (0.2 ≤ y ≤ 0.8) Cathode Materials for Rechargeable Lithium-Ion Batteries: Their Understanding. *Chem. Mater.* **25**, 1121–1131 (2013).
 33. Armstrong, A. R. *et al.* Demonstrating Oxygen Loss and Associated Structural Reorganization in the Lithium Battery Cathode Li[Ni_{0.2}Li_{0.2}Mn_{0.6}]O₂. *J. Am. Chem. Soc.* **128**, 8694–8698 (2006).
 34. Lee, K. T. K. T. *et al.* P₂-type Na_x[Fe_{1/2}Mn_{1/2}]O₂ made from earth-abundant elements for rechargeable Na batteries. *Chem. Mater.* **26**, 820–829 (2014).
 35. Mortemard De Boisse, B., Carlier, D., Guignard, M., Bourgeois, L. & Delmas, C. P₂-Na_xMn_{1/2}Fe_{1/2}O₂ phase used as positive electrode in Na batteries: Structural changes induced by the electrochemical (De)intercalation process. *Inorg. Chem.* **53**, 11197–11205 (2014).
 36. Jiang, M., Key, B., Meng, Y. S. & Grey, C. P. Electrochemical and Structural Study of the Layered, ‘Li-Excess’ Lithium-Ion Battery Electrode Material Li[Li_{1/9}Ni_{1/3}Mn_{5/9}]O₂. *Chem. Mater.* **21**, 2733–2745 (2009).

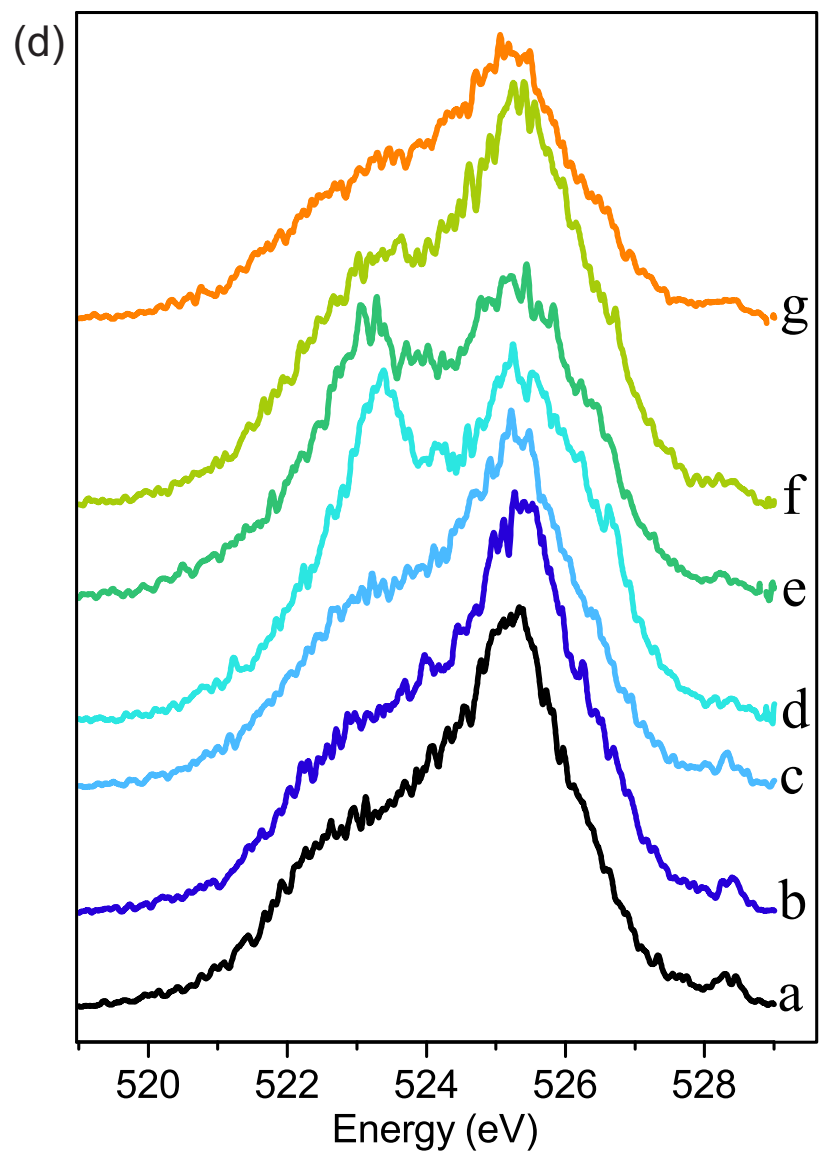
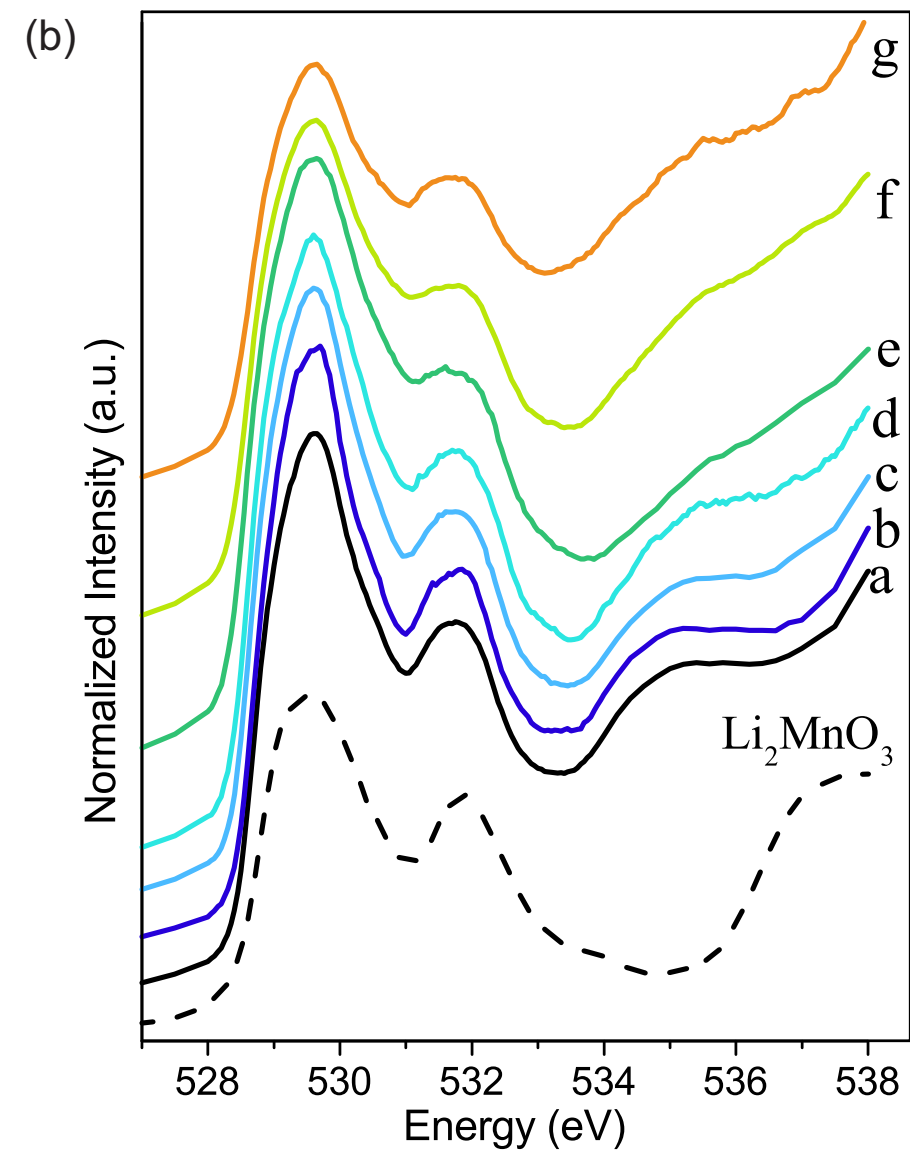
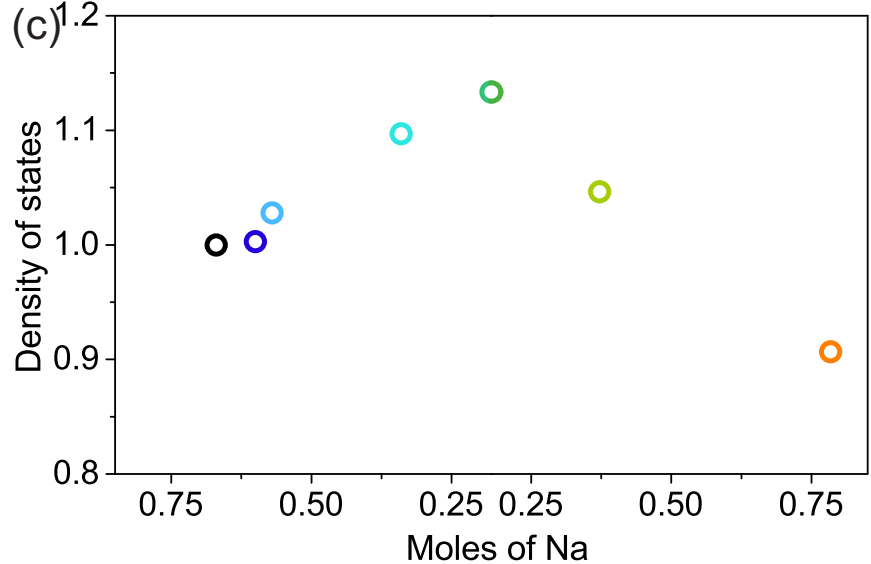
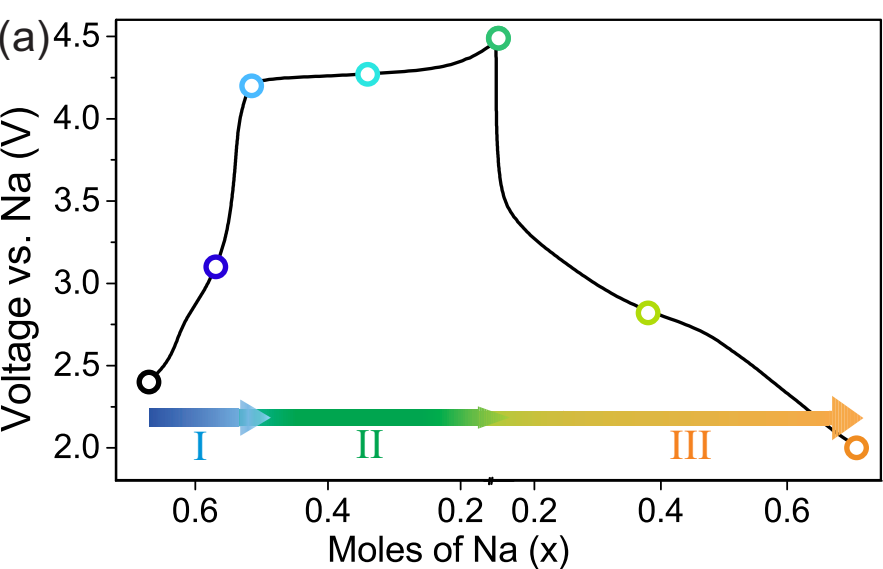
37. Xu, J. *et al.* Identifying the Critical Role of Li Substitution in $\text{P2-Na}_x[\text{Li}_y\text{Ni}_z\text{Mn}_{1-y-z}]\text{O}_2$ ($0 < x, y, z < 1$) Intercalation Cathode Materials for High-Energy Na-Ion Batteries. *Chem. Mater.* **26**, 1260–1269 (2014).
38. Ghiringhelli, G., Braicovich, L., Schmitt, T. & Strocov, V. High-resolution RIXS with the SAXES Spectrometer at the ADRESS Beamline of the Swiss Light Source. *Synchrotron Radiat. News* **25**, 16–22 (2012).
39. Strocov, V. N. *et al.* High-resolution soft X-ray beamline ADRESS at the Swiss Light Source for resonant inelastic X-ray scattering and angle-resolved photoelectron spectroscopies. *J. Synchrotron Radiat.* **17**, 631–643 (2010).
40. Ghiringhelli, G. *et al.* SAXES, a high resolution spectrometer for resonant x-ray emission in the 400-1600 eV energy range. *Rev. Sci. Instrum.* **77**, (2006).



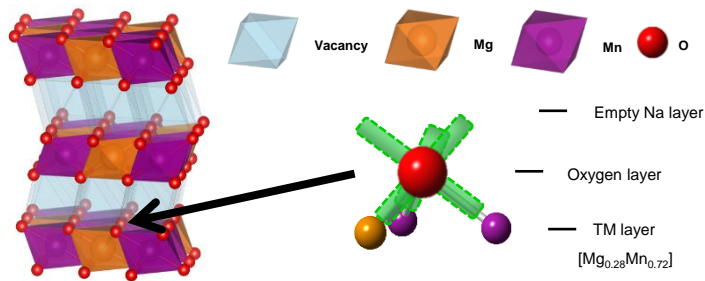




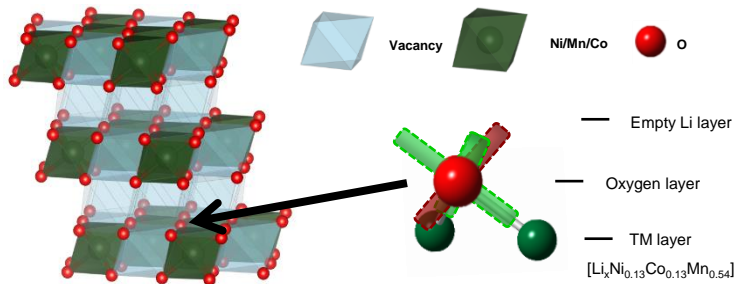




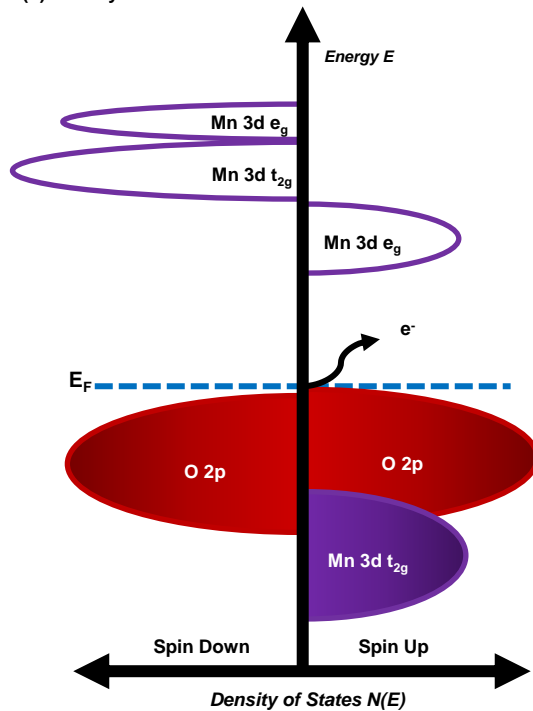
(a) O2-type $\text{Na}_0[\text{Mg}_{0.28}\text{Mn}_{0.72}]\text{O}_2$

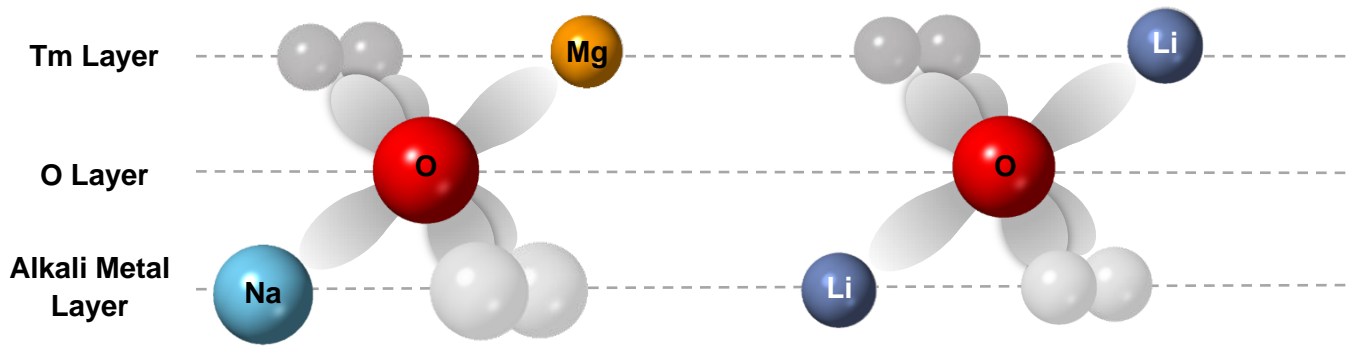


(c) $\text{Li}_0[\text{Li}_x\text{Ni}_{0.13}\text{Co}_{0.13}\text{Mn}_{0.54}]\text{O}_2$ ($x < 0.2$)



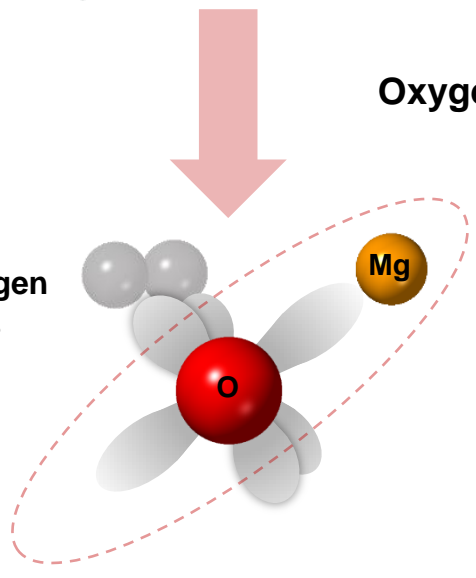
(b) Density of States





Oxygen Oxidation

No Oxygen Loss



Oxygen Loss

